

# Tracing the Milky Way spiral arms with $^{26}\text{Al}$ .

## The role of nova systems in the 2D distribution of $^{26}\text{Al}$

A. Vasini <sup>1,2</sup> \*, E. Spitoni <sup>2</sup>, F. Matteucci <sup>1,2,3</sup>, G. Cescutti <sup>1,2,3</sup>, and M. Della Valle <sup>4,5</sup>

<sup>1</sup> Dipartimento di Fisica, Sezione di Astronomia, Università di Trieste, Via G. B. Tiepolo 11, I-34143 Trieste, Italy

<sup>2</sup> I.N.A.F. Osservatorio Astronomico di Trieste, via G.B. Tiepolo 11, 34131, Trieste, Italy

<sup>3</sup> I.N.F.N. Sezione di Trieste, via Valerio 2, 34134 Trieste, Italy

<sup>4</sup> INAF - Osservatorio Astronomico di Capodimonte, Salita Moiarriello 16, I-80131, Napoli, Italy

<sup>5</sup> ICRANet, Piazza della Repubblica 10, I-65122 Pescara, Italy

Received xxxx / Accepted xxxx

### ABSTRACT

**Context.** Massive stars are one of the most important and investigated astrophysical production sites of  $^{26}\text{Al}$ , a short-lived radioisotope with  $\sim 1$  Myr half-life. Its short lifetime prevents us from observing its complete chemical history, and only the  $^{26}\text{Al}$  that was recently produced by massive stars can be observed. Hence, it is considered a tracer of star formation rate (SFR). However, important contributions to  $^{26}\text{Al}$  comes from nova systems that pollute the interstellar medium with a large delay, thus partly erasing the correlation between  $^{26}\text{Al}$  and SFR.

**Aims.** In this work we describe the 2D distribution of the mass of  $^{26}\text{Al}$  as well as that of massive stars and nova systems in the Milky Way, to investigate their relative contributions to the production of  $^{26}\text{Al}$ .

**Methods.** We use a detailed 2D chemical evolution model where the SFR is azimuthally dependent and is required to reproduce the spiral arm pattern observed in the Milky Way. We test two different models, one where the  $^{26}\text{Al}$  comes from massive stars and novae, and one with massive stars only. We then compare the predictions to the  $\sim 2 M_{\odot}$  of  $^{26}\text{Al}$  mass observed by the surveys COMPTEL and INTEGRAL.

**Results.** The results show that novae do not trace SFR and, in the solar vicinity, they concentrate in its minima. The effect of novae on the map of the  $^{26}\text{Al}$  mass consists in damping the spiral pattern by a factor of five. Regarding the nucleosynthesis, we find that  $\sim 75\%$  of the  $^{26}\text{Al}$  is produced by novae and the  $\sim 25\%$  by massive stars.

**Conclusions.** We conclude that novae cannot be neglected as  $^{26}\text{Al}$  producers since the observations can only be reproduced by including their contribution. Moreover, we suggest that bulge novae should eject around six times more material than the disc ones to well reproduce the observed mass of  $^{26}\text{Al}$ .

**Key words.** Galaxy: bulge – Galaxy: disk – Galaxy: abundances – Galaxy: evolution – Stars: Novae – Gamma rays: diffuse background

## 1. Introduction

Short-lived radioisotopes (SLRs) are a class of nuclei that undergo a radioactive decay occurring on very short astronomical timescales ( $\sim 1$ -10 Myr). They represent the link between different approaches to unveil the processes behind Galactic evolution, from chemical evolution (Timmes et al. 1995) to the measurements of the isotopical abundances in meteorites coming from the solar neighbourhood (Desch et al. 2023). Other theoretical methods tested were the simulations of the superbubbles (Schulreich et al. 2023), Galactic population synthesis models (Siebert et al. 2023) and the stochastic chemical evolution studies such as those presented in Côté et al. (2019a,b). Given their brief half-life, these nuclei rapidly decay into the final product of their decay chain, leaving behind no trace of their previous presence. Therefore, all the measurements and the theoretical studies addressed to SLRs focus on the present day scenario only, because no heritage of the past history is left.

The astronomical interest behind  $^{26}\text{Al}$  lies also in its close relation to the star formation rate (SFR). Since, generally, massive stars have been considered as the main source of  $^{26}\text{Al}$ , this

isotope is restored into the interstellar medium (ISM) shortly after the birth of its stellar progenitor. Moreover, its short decay timescale prevents  $^{26}\text{Al}$  from moving too far away from the location of the progenitor. As a consequence, since massive stars are located in the active star formation regions of the Galaxy, this isotope will also be detected in the proximity of these areas. Hence,  $^{26}\text{Al}$  has been considered a good tracer of star formation regions (Limongi & Chieffi 2006).

In the past, chemical evolution studies relative to SLRs, tried to reproduce the observations provided in the last decades by the  $\gamma$ -ray astronomy community (Vasini et al. 2022; Wehmeyer et al. 2023) and offered predictions for upcoming observations of external structures (Vasini et al. 2023).

Many of these results were obtained by means of 1D chemical evolution models which assume that every observable (such as the SFR, the infall rate, the gas and stellar masses and the abundance gradients) depends only on the radial coordinate. Hence, the Milky Way (MW) is modeled by assuming a concentric ring structure, where the gas in each ring instantaneously and homogeneously mixes (instantaneous mixing approximation).

The picture becomes more complex when dealing with SLRs since an additional timescale is introduced, namely the timescale

\* email to: arianna.vasini@inaf.it

of their radioactive decay, and in this particular case that of  $^{26}\text{Al}$  ( $\sim 1$  Myr, see [Diehl 2013](#)).  $^{26}\text{Al}$ , after being re-injected into the ISM, starts spreading in the surrounding regions as stable isotopes also do but, simultaneously, it also decays into  $^{26}\text{Mg}$ . As a consequence, the  $^{26}\text{Al}$  atoms will not mix homogeneously, because the mixing timescale is very likely longer than the  $^{26}\text{Al}$  decay timescale. Therefore, for  $^{26}\text{Al}$ , such as for other SLRs, the assumption of homogeneous mixing does not hold anymore. This fact would not be a problem if the SFR in the Galaxy was homogeneous but, as observations confirm, the SFR is concentrated in the spiral arms of the MW. Therefore a 1D chemical evolution model that assumes homogeneous mixing is not suitable for dealing with SLRs in the Galaxy. The solution is introducing a second dimension, namely the azimuth, in order to trace inhomogeneities in each ring.

Moreover, the scenario is further complicated by the part played by the nova systems, that represent a second but non negligible source of  $^{26}\text{Al}$  ([Nofar et al. 1991](#)). The chemical enrichment from novae is characterized by a long time delay due to the combination of the time necessary to form a white dwarf and the additional cooling time requested to trigger the nova explosion ([D'Antona & Matteucci 1991](#)). The direct consequence of this is that novae, unlike massive stars, do not trace the SFR. Given that a fraction of the  $^{26}\text{Al}$  in the Galaxy has a nova origin, the  $^{26}\text{Al}$ -SFR correlation is necessarily reduced, even though it is not yet clear how much. To determine the damping due to the nova contribution, a 2D chemical evolution model is needed.

[Spitoni et al. \(2019, 2023\)](#) proposed a 2D chemical evolution model where azimuth and radial coordinates were considered. The azimuth is introduced by perturbing the SFR so as to reproduce the MW spiral arms. In these papers, every ring is divided into smaller cells, and the homogeneity is not imposed over the whole ring but rather over the single cells. This updated scenario allows the authors to show clearly that the 1D models represent a valid alternative almost everywhere in the Galaxy, except when dealing with the co-rotational radii regions where oscillations in chemical abundances over cells in the same ring arise and only the 2D model can trace them.

From the observational side, evidences of SLRs in the Galaxy have been collected adopting  $\gamma$ -ray astronomy techniques. Since 1991 two surveys, at first COMPTEL ([Schönfelder et al. 1984; Diehl et al. 1995](#)) and later INTEGRAL ([Winkler 1994; Pleintinger et al. 2023](#)), have been dedicated to exploring the distribution of these elements along different longitudes on the Galactic plane and different latitudes above and below the Galactic plane. Among the most important results that were provided there is the 2D cartography of the  $^{26}\text{Al}$  in the MW (see [Plüschke et al. 2001; Diehl & Prantzos 2023](#)) where the evidence of a diffuse emission on the Galactic plane is reported together with some localized star formation regions superimposed. From the same data, also integrated measurements of the mass of  $^{26}\text{Al}$  in the region included within 5 kpc from the Galactic center were provided. [Prantzos & Diehl \(1996\)](#), adopting the flux measurements from COMPTEL, estimated an  $^{26}\text{Al}$  mass between 1.5 and 2  $M_{\odot}$  within 5 kpc from the Galactic center, whereas by making use of the measurements from INTEGRAL [Diehl \(2016\)](#) proposed  $2.0 \pm 0.3 M_{\odot}$  in the same 5 kpc radius ring. In [Vasini et al. \(2022\)](#) we already provided a theoretical estimate of  $^{26}\text{Al}$  integrated over that same region by adopting a 1D chemical evolution model to reproduce the disc and the bulge separately. With the prescriptions adopted, we were able to reproduce the observations and constrain the stellar yields, showing that a non negligible contribution from novae is necessary. A yet unexplored question is how much the

integrated values are influenced by the adoption of a 1D rather than a 2D model. A 2D model, as already explained above, would be able to trace the oscillations in the SFR across the MW, at variance with a 1D model. Moreover, regarding the integrated values within the region of interest no conclusions can be drawn until a suitable 2D chemical evolution model for radioactive isotopes is developed.

With this work we want to provide a 2D chemical evolution model to follow the evolution in space (as a function of radial distance and azimuth) and time of  $^{26}\text{Al}$  in the MW by adding an azimuth-dependent perturbation to the SFR that resembles the spiral arm pattern observed. Our aim is to showcase the impact of the nova population on the present day distribution of this isotope. Moreover, with our model we can hopefully have deeper insights on the differences between the novae in the bulge and in the disc, by modeling these two regions separately.

The paper is organized as follows. In Sec. 2 we present the chemical evolution model adopted starting from the original 1D version for thick and thin discs and the bulge, and then we move to the nucleosynthesis considered with the description of the two models tested. In Sec. 3 we show how we extended the 1D model by adding the azimuthal dependency to the SFR, then in Sec. 4.5 we show the Galactic observational constraints that we can reproduce. We present our results about novae and  $^{26}\text{Al}$  in Sec. 4 and, finally, we summarize our main conclusions in Sec. 5.

## 2. The reference 1D chemical evolution model

In this Section, we present the reference 1D chemical evolution model that we use as starting point for this work. The 2D extension will be described later in Sec. 3.

We use as reference model the one adopted in [Vasini et al. \(2022\)](#). The Galaxy is composed of two separated regions, the bulge (up to 2 kpc from the Galactic center) and the disc (from 2 kpc to 15 kpc from the MW center), itself composed of two chemically distinct substructures, the thick disc and the thin disc.

The thin disc is divided in 1 kpc wide concentric rings, that are isolated from each other since we neglect every radial gas flow. The bulge as well is modeled by assuming a central region until 1 kpc from the center and a surrounding ring, from 1 kpc to 2 kpc. Moreover, in the 1D model each ring is chemically homogeneous.

### 2.1. Galactic thick and thin discs

We assume that thick and thin discs form out of gas coming from two different infall episodes according to:

$$A(R, t) = a(R)e^{-t/\tau_T} + b(R)e^{-(t-t_{\max})/\tau_D(R)}, \quad (1)$$

where the first episode is responsible of the formation of the thick disc on a timescale  $\tau_T=1.0$  Gyr, whereas the thin disc is formed by the second infall following an "inside-out" scenario (see [Matteucci & Francois 1989](#)). To reproduce that, the second infall timescale is dependent on the Galactocentric distance following the law  $\tau_D(R) = 1.033 (R/\text{kpc}) - 1.267$  Gyr ([Chiappini et al. \(2001\)](#)). Additionally,  $t_{\max} = 1$  Gyr represents the time of maximum infall in the second accretion episode, indicating the delay between the end of the first and the start of the second infall episode. The parameters  $a(R)$  and  $b(R)$  are adjusted to match the current total surface mass density of the thick and thin discs, set to  $17 M_{\odot} \text{pc}^{-2}$  and  $54 M_{\odot} \text{pc}^{-2}$ , respectively ([Chiappini et al.](#)

2001). A similar mechanism for the growth of the Galactic assembling mass is identified in cosmological simulations (Brook et al. 2012; Bird et al. 2013; Vincenzo & Kobayashi 2020).

The SFR is expressed as the Kennicutt (1998) law:

$$\psi(R, t) \propto \nu(R) \Sigma_{\text{gas}}^k(R, t), \quad (2)$$

where  $\nu(R)$  is the star formation efficiency that we assume to be  $1.0 \text{ Gyr}^{-1}$  everywhere in the Galaxy, the same for thick and thin discs and  $\Sigma_{\text{gas}}$  is the surface gas mass density.

We assume a Kroupa et al. (1993) IMF with three slopes, defined in a mass interval up to  $100 M_{\odot}$ :

$$\varphi_{\text{K93}}(M) \propto \begin{cases} M^{-1.3} & M < 0.5 M_{\odot} \\ M^{-2.2} & 0.5 < M/M_{\odot} < 1 \\ M^{-2.7} & M > 1 M_{\odot}. \end{cases} \quad (3)$$

Regarding the stellar contribution to the ISM chemical composition, our model accounts for stars in different mass ranges, hence with different explosion mechanisms and lifetimes.

The stars from  $M_L=8 M_{\odot}$  up to  $M_U=30 M_{\odot}$  die as Type II Supernovae (Type II SNe) whereas the more massive ones, from  $M_L=30 M_{\odot}$  up to  $M_U=100 M_{\odot}$  die as Type Ib SNe or Type Ic SNe. These SNe are all core-collapse ones and their rate can be written as:

$$R_{\text{SNII,Ib,Ic}}(t) = \int_{M_L}^{M_U} \psi(t - \tau_m) \varphi(m) dm, \quad (4)$$

where the  $\tau_m$  is the lifetime of a star of mass  $m$ .

On the other hand, the Type Ia SNe follow the single degenerate scenario from Matteucci & Greggio (1986) and Matteucci & Recchi (2001), with the following rate:

$$R_{\text{SNIa}}(t) = A_B \int_{M_{\text{Bm}}}^{M_{\text{BM}}} \varphi(m) \left[ \int_{\mu_{\text{Bmin}}}^{0.5} f(\mu_B) \psi(t - \tau_{m2}) \right] dm. \quad (5)$$

The parameters are set as follows.  $A_B$  is the fraction of binary systems that can generate a Type Ia SNe progenitor and it depends on the chosen IMF. In our case  $A_B = 0.09$ . The mass  $m$  over which the integration is performed is the total mass of the binary system, so as  $M_{\text{Bm}}$  and  $M_{\text{BM}}$  are the smallest and the largest possible total mass of the system, respectively. To generate a SNIa the two companions should be massive enough to make the white dwarf reach the Chandrasekhar mass, therefore we set  $M_{\text{Bm}} = 3 M_{\odot}$ .  $M_{\text{BM}}$  is instead set to  $16 M_{\odot}$  because the upper limit to form a CO white dwarf is  $8 M_{\odot}$ .  $f(\mu_B)$  is the distribution of the mass ratio between the two stars, and  $\psi(t - \tau_{m2})$  is the SFR at the time of formation of the secondary star, which represents the clock of the system.

Moreover, we also consider the contribution from nova systems, that are of particular interest in this case. They are implemented according to D'Antona & Matteucci (1991):

$$R_{\text{novaout}}(t) = 10^4 \cdot \alpha \int_{0.8}^8 \psi(t - \tau_m - \Delta t) \varphi(m) dm, \quad (6)$$

where  $\alpha$  is the fraction of binary systems that are able to generate a nova, that was set to 0.0115. With this value we are able to reproduce the current nova rate in the MW disc.  $\psi(t - \tau_m - \Delta t)$  is the SFR at the formation of the binary system. The delay between the nova explosion and its birth is given by the sum of two contributions,  $\tau_m$ , its lifetime, and the time needed for the white dwarf to cool down,  $\Delta t$ , set to 1.0 Gyr. In addition, the factor  $10^4$  accounts for the several explosions that each nova system undergo during its lifetime (see Ford 1978). The explosions of a nova system are distributed in time and should be modeled accordingly. This aspect has already been analysed by Cescutti & Molaro (2019) that improved the scenario by adopting multiple explosions, but did not find significant differences.

## 2.2. The bulge

Assuming that the Galactic bulge resides in the innermost region, within 2 kpc from the Galactic center, we model it separately, following the prescriptions from Matteucci et al. (2019). We divide it into a disc, from the center up to 1 kpc, and an external ring, from 1 kpc to 2 kpc, so that the concentric rings throughout the entire Galaxy are all equally thick.

The gas forming the bulge is all accreted from a single infall episode according to:

$$A(R, t) = a(R) e^{-t/\tau_B} \quad (7)$$

where the timescale  $\tau_B$  is set to 0.1 Gyr (Ballero et al. 2007).  $a(R)$ , as in the case of the disc, is a free parameter whose value is chosen to reproduce the mass density of the inner and the outer bulge regions,  $\sim 1970 M_{\odot} \text{ pc}^{-2}$  and  $\sim 1350 M_{\odot} \text{ pc}^{-2}$ , in agreement with Ballero et al. (2007) and Grieco et al. (2012).

Concerning the SFR, we adopt the same law as in 2 with an efficiency  $\nu$  of  $25.0 \text{ Gyr}^{-1}$  and  $35.0 \text{ Gyr}^{-1}$  for the ring and the inner region, respectively. This large star formation efficiency, together with the short timescale of the SFR, reproduces the rapid increase in the metallicity and the average old stellar population observed in the bulge nowadays (Barbuy et al. 2018).

The assumed IMF is the one of Salpeter (1955):

$$\varphi(M) \propto M^{-2.35}. \quad (8)$$

We choose such an IMF since it was demonstrated in previous papers that the IMF in the bulge should be top heavier than the disc IMF (Matteucci & Brocato 1990; Ballero et al. 2007; Cescutti & Matteucci 2011). The rates of the different stellar types, SNe Ia, II, Ib and Ic are the same as in the disc, whereas in the nova rate (see eq. 6) the value  $\alpha$  is set to 0.024 since it depends on the IMF of choice.

## 2.3. Nucleosynthesis prescriptions

For the nucleosynthesis prescriptions we rely on the yields already selected in Vasini et al. (2022). For massive stars we assume yields from Kobayashi et al. (2006), to which we add those for  $^{26}\text{Al}$  from Woosley & Weaver (1995) adopting the whole metallicity grid provided. For nova systems we use José & Hernanz (2007) that report different models regarding the nova composition (CO or ONe novae). To consider the full spectrum of possibilities in the nova population we assume that 70% are CO novae and the remaining 30% is composed of ONe novae. In addition, in the two cases, several yields are provided depending on the initial mass of the white dwarf. Therefore, the yield that we chose is the average of those proposed. This assumption is taken from Romano & Matteucci (2003) and can be summarized as:

$$\langle X_{\text{nova}} \rangle = 0.7 \langle X_{\text{CO}} \rangle + 0.3 \langle X_{\text{ONe}} \rangle. \quad (9)$$

The resulting nova yield is  $7.69 \times 10^{-4} M_{\odot}$ . For SNIa we assume yields from Iwamoto et al. (1999) and for  $^{26}\text{Al}$  we adopt the prescriptions from Nomoto et al. (1984). Moreover, for AGBs ( $M \leq 6 M_{\odot}$ ) we adopt the yields from Karakas (2010).

In this work we test two different models that differ only for the nucleosynthesis prescriptions summarized in Table 1: Model 1 consider the production of  $^{26}\text{Al}$  from all the sources listed (massive stars and novae with minor contribution coming from SNIa and AGBs), and Model 2 where we exclude the contribution from novae, keeping massive star, AGBs and SNIa.



Model	Massive stars	Novae	AGBs	SN Ia
Model 1	✓	✓	✓	✓
Model 2	✓	✗	✓	✓

**Table 1.** Descriptions of the nucleosynthesis of the two models tested. The checkmarks mark the  $^{26}\text{Al}$  sources included in the models. For the reference to the yields adopted for each astrophysical source see Sec. 2.3.

### 3. The 2D chemical evolution model

To extend our model from 1D to 2D, we include the azimuthal dimension by adopting the same mechanism proposed by [Spitoni et al. \(2019, 2023\)](#), where SFR perturbation are implemented in order to reproduce the spiral arm pattern observed in the MW. In this Section we show how the spiral patterns are modeled and then how they are introduced in the SFR.

#### 3.1. Multiple spiral patterns of Spitoni+23

[Spitoni et al. \(2023\)](#) presents the chemical evolution of several elements in the Galactic disc, considering the effects of multiple spiral patterns on the evolution of elements synthesized over different time scales, such as oxygen, iron, europium, and barium. The presence of multiple spiral patterns was already predicted by N-body simulations ([Quillen et al. 2011](#); [Minchev et al. 2012](#); [Sellwood & Carlberg 2014](#)) and shown by observations ([Meidt et al. 2009](#)).

The expression for the time evolution of the density perturbation, created by multiple pattern spiral arms is:

$$\Sigma_{MS}(R, \phi, t) = \chi(R, t) \sum_{j=1}^N M_j(\gamma_j) \cdot \mathbb{1}[R_{j,\min}, R_{j,\max}], \quad (10)$$

where the quantity  $\chi(R, t)$  if computed at the present time  $t_G$ , represents the present-day amplitude of the spiral density and can be expressed as:

$$\chi(R, t_G) = \Sigma_{S,0} e^{-\frac{R-R_0}{R_S}}. \quad (11)$$

In the previous expression,  $R_S$  is the radial scale-length of the drop-off in density amplitude of the arms,  $\Sigma_0$  is the surface arm density at fiducial radius  $R_0$  fixed to values of  $\Sigma_{S,0} = 20 \text{ M}_\odot \text{ pc}^{-2}$ ,  $R_0 = 8 \text{ kpc}$ , and  $R_S = 7 \text{ kpc}$  as in [Spitoni et al. \(2023\)](#) and [Cox & Gómez \(2002\)](#). In eq. 10,  $N$  is the total number of spiral clumps and the  $M_j(\gamma_j)$  term is the modulation function for concentrated spiral arms of [Cox & Gómez \(2002\)](#) defined for the  $j^{\text{th}}$  spiral mode clump associated with the angular velocity  $\Omega_{s,j}$  and can be expressed as follows:

$$M_j(\gamma_j) = \left( \frac{8}{3\pi} \cos(\gamma_j) + \frac{1}{2} \cos(2\gamma_j) + \frac{8}{15\pi} \cos(3\gamma_j) \right), \quad (12)$$

where  $\gamma_j$  stands for

$$\gamma_j(R, \phi, t) = m_j \left[ \phi + \Omega_{s,j} \cdot t - \phi_p(R_0) - \frac{\ln(R/R_0)}{\tan(\alpha)} \right]. \quad (13)$$

In eq. 13,  $m_j$  refers to the multiplicity (e.g. the number of spiral arms) associated to the  $j^{\text{th}}$  clump,  $\alpha$  is the pitch angle<sup>1</sup>,  $\Omega_{s,j}$  is

<sup>1</sup> In this model all the spiral arms have the same pitch angle  $\alpha$ .

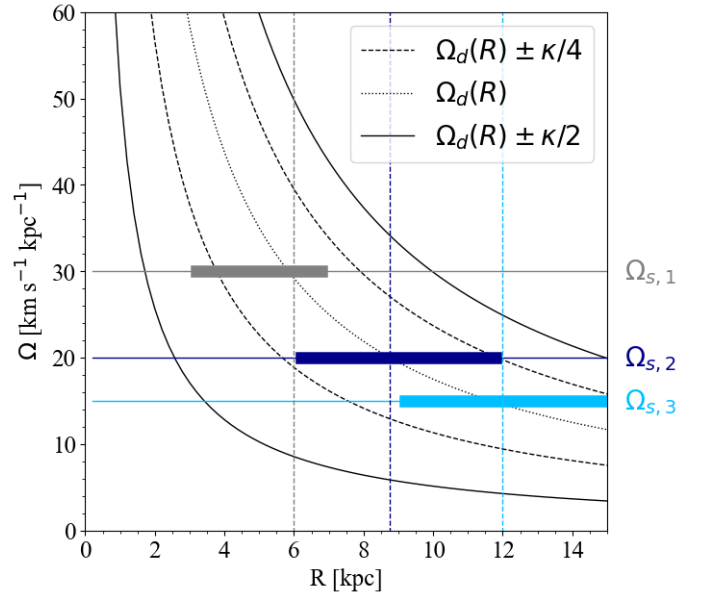


**Fig. 1.** Spiral pattern speeds  $\Omega_{s,1}(R)$ ,  $\Omega_{s,2}(R)$  and  $\Omega_{s,3}(R)$  of the multiple spiral modes moving at different pattern speeds of Model A in [Spitoni et al. \(2023\)](#) are indicated by the three coloured horizontal lines. Inner and outer spiral structures (moving with the above-mentioned pattern speeds) are also indicated by the thicker grey, blue and green light-blue, respectively. The disc angular velocity  $\Omega_d(R)$  computed by [Roca-Fàbrega et al. \(2014\)](#) is indicated with the dotted line. The 2:1 and 4:1 outer and inner Lindblad resonances (OLR and ILR) occur along the solid and dashed black curves, respectively. Resonances have been computed as  $\Omega_{p2}(R) = \Omega_d(R) \pm \kappa/2$  and  $\Omega_{p4}(R) = \Omega_d(R) \pm \kappa/4$ , respectively where  $\kappa$  is the local radial epicyclic frequency. The long vertical dashed lines show the positions of the co-rotation radii assuming the three different  $\Omega_s$  values.

the angular velocity of the pattern,  $\phi_p(R_0)$  is the coordinate  $\phi$  computed at  $t=0 \text{ Gyr}$  and  $R_0$ .

Finally, in eq. 10, the value of the indicator function  $\mathbb{1}$  delimits the radial extension of the considered spiral arm mode enclosed between the Galactocentric distances  $R_{j,\min}$  and  $R_{j,\max}$ : it is one if the argument is within the radial interval and zero otherwise.

In Fig. 1, we show the pattern speeds  $\Omega_{s,j}(R)$  of the spiral arms of Model A in [Spitoni et al. \(2023\)](#), which we adopt in this work. The spiral structure is composed of three segments with multiplicity  $m = 2$ , each moving at different pattern speeds  $\Omega_{s,j}(R)$ . The  $j^{\text{th}}$  spiral structure is confined to the region  $R \in [R_{j,\min}, R_{j,\max}]$ . The velocity of the central spiral structure is fixed at  $\Omega_{s,2} = 20 \text{ km s}^{-1} \text{ kpc}^{-1}$ , consistent with the [Roca-Fàbrega et al. \(2014\)](#) model. A similar value was first estimated from moving groups in the U-V plane by [Quillen & Minchev \(2005,  \$\Omega = 18.1 \pm 0.8 \text{ km s}^{-1} \text{ kpc}^{-1}\$ \)](#). The innermost and outermost segments rotate at velocities of  $\Omega_{s,1} = 30 \text{ km s}^{-1} \text{ kpc}^{-1}$  and  $\Omega_{s,3} = 15 \text{ km s}^{-1} \text{ kpc}^{-1}$ , respectively.

It is interesting to note that one of the co-rotational radii is located at 8.75 kpc, which is close to the solar Galactocentric distance  $(R, Z)_\odot = (8.249, 0.0208) \text{ kpc}$  ([GRAVITY Collaboration et al. 2021](#); [Bennett & Bovy 2019](#)).

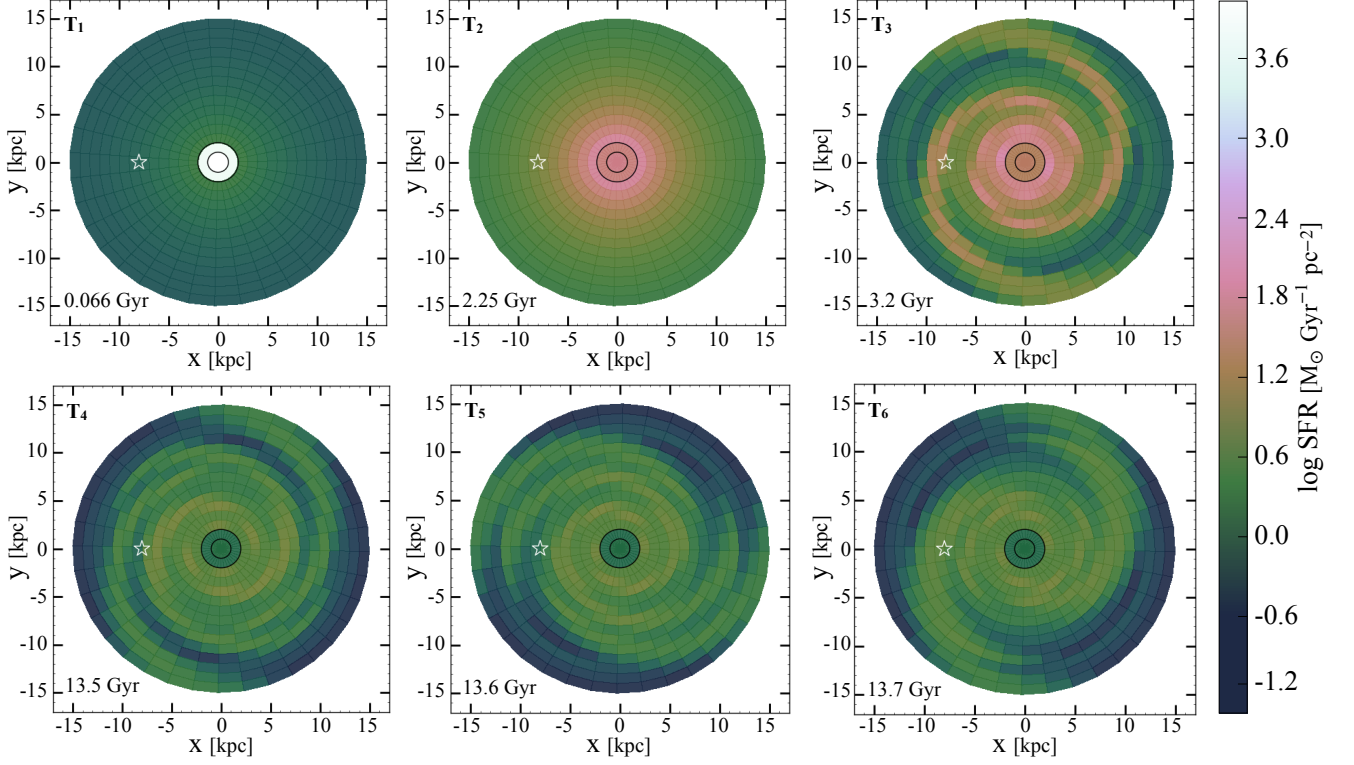


**Fig. 2.** 2D SFR from the bulge to the outskirts of the MW (assumed in this paper to be 15kpc). Here we report six snapshots at different time steps during the MW evolution:  $T_1=0.066$  Gyr (the peak of the bulge SFR),  $T_2=2.25$  Gyr (the peak of the disk SFR),  $T_3=3.2$  Gyr (right after the onset of the spiral arms), two recent times,  $T_4=13.5$  Gyr and  $T_5=13.6$  Gyr, and the present day time, assumed to be  $T_6=13.7$  Gyr. The position of the sun is represented by the white-edge star.

### 3.2. SFR and perturbations

We first present the assumptions adopted for the SFR and for the spiral arms in the disc ( $R > 2$  kpc), since the other chemical evolution prescriptions depend on those.

Our starting point is a 1D SFR depending only on the Galactocentric distance  $R$  and following a Schmidt-Kennicutt law (Kennicutt 1998):

$$\psi(R, t) \propto \nu(R) \Sigma_{\text{gas}}^k(R, t), \quad (14)$$

where  $\nu$  and  $\Sigma_{\text{gas}}$ , the star formation efficiency and the surface gas mass density respectively, both depend on the Galactocentric distance, whereas  $k = 1.5$  everywhere in the disc.

This relation is still mono-dimensional, meaning that we have not introduced a dependency on the azimuthal angle yet.

We define the adimensional perturbation  $\delta_{MS}$  as:

$$\delta_{MS}(R, \phi, t) \equiv \frac{\Sigma_D(R, t) + \Sigma_{MS}(R, \phi, t)}{\Sigma_D(R, t)}, \quad (15)$$

where  $\Sigma_D$  is the total surface mass density. Imposing as in Spitoni et al. (2023) that the ratio  $\chi(R, t)/\Sigma_D(R, t)$  is constant in time, the adimensional perturbation  $\delta_{MS}$  defined above becomes:

$$\delta_{MS}(R, \phi, t) = 1 + \frac{\chi(R, t_G)}{\Sigma_D(R, t_G)} \sum_{j=1}^N M_j(\gamma_j) \cdot \mathbb{1}[R_{j,\min}, R_{j,\max}], \quad (16)$$

Finally, the new SFR in presence of the effect of spiral arms is computed as:

$$\psi(R, t, \phi) \propto \nu(R) \Sigma_{\text{gas}}^k(R, t) \cdot \delta_{MS}^k(R, \phi, t). \quad (17)$$

We apply the perturbation after 3 Gyr of evolution and then we let the MW evolve up to 13.7 Gyr, the assumed age of the Universe. We make this choice in order to mimic what is done in Spitoni et al. (2019). They simulate the 2D evolution of the thin disc only, assuming a one-infall episode lasting for 11 Gyr. In our case, where we model both the thin and the thick discs in the framework of a two-infall scenario for 13.7 Gyr, we delay the rising of the perturbation by 3 Gyr relative to the beginning of the star formation, so that also in our case the evolution of the perturbation lasts for roughly 11 Gyr.

We show our perturbed SFR in Fig. 2. We represent both the bulge ( $R \leq 2$  kpc) and the disc at six different times using the same color coding so as to appreciate the SFR variations in time and space. In the top row, starting from the left panel the snapshots shown are those corresponding to the peak of the bulge SFR ( $T_1=0.066$  Gyr), the peak of the disk SFR ( $T_2=2.25$  Gyr), and the rising of the SFR perturbations ( $T_3=3.2$  Gyr). Regarding the bottom panels, when dealing with short-lived radioisotopes as  $^{26}\text{Al}$  the observations can recover only the recent history which is related to the recent SFR, therefore we show three recent times ( $T_4=13.5$  Gyr,  $T_5=13.6$  Gyr and  $T_6=13.7$  Gyr) to hopefully trace their SFR when analyzing the  $^{26}\text{Al}$  distribution. The white edge star shows the locations of the the solar neighbourhood.

In the  $T_1$  panel we show that when the bulge SFR reaches a maximum, the disc SFR is still very low, roughly four order of magnitudes lower. Then, at  $T_2$ , the bulge SFR has already decreased since it is characterized by an extremely efficient and short burst whereas the disc SFR shows a spike, whose value is

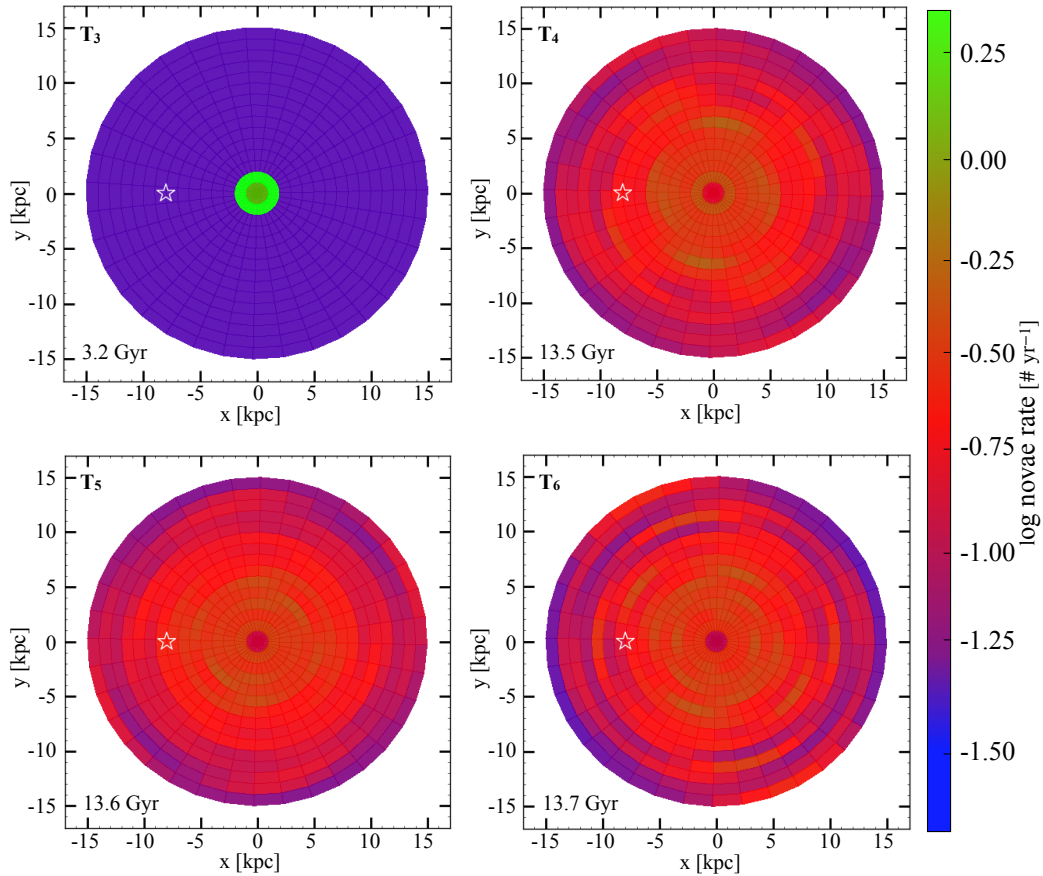


**Fig. 3.** 2D map of nova outburst rate in the MW at four different times,  $T_3$ ,  $T_4$ ,  $T_5$  and  $T_6$ .

smaller and smaller as we go towards the outskirts. At  $T_3$  the perturbations arise and are clearly visible in the disc since this is the moment when they are at their peak. After this moment the SFR perturbations will monotonically decrease. In the three bottom panels ( $T_4$ ,  $T_5$  and  $T_6$ ) the perturbations are still evident, although quite weaker, and the different segments that compose the single arms are not aligned due to their different rotational velocities. The result is that the arms look broadened as it is particularly evident in the last panel.

## 4. Results

In this Section we show the results regarding the nova and  $^{26}\text{Al}$  2D distribution in the MW, from the bulge up to the outermost region of the Galaxy.

### 4.1. Nova systems

In this Section we show the results related to the nova outbursts in the MW.

In Fig. 3 we report the 2D map of the novae for four of the six times shown in Fig. 2. The four panels refer to times  $T_3$ ,  $T_4$ ,  $T_5$  and  $T_6$  as defined in Sec. 3.2. We do not show the snapshots at  $T_1$  and  $T_2$  since at such early epochs novae have not started to explode yet. The maps are color coded according to the logarithm of the nova outburst rate, and the solar ring at 8 kpc is marked by the white-edge star in the left side of each panel.

The difference between the early epoch ( $T_3$ ) and the recent ones ( $T_4$ ,  $T_5$  and  $T_6$ ) is evident. The reason, as anticipated, lies in the delay time distribution of the novae.

Because of this delay, novae do not trace the SFR, and no correspondence can be found between the 2D SFR map and the 2D nova map computed at the same epoch. Therefore, at  $T_3$  the nova distribution is still uniform, even though the SFR is already perturbed, and at late epochs novae do not show the spiral arm pattern which is shown by the SFR.

The same time delay affects the bulge novae but the result in this region is slightly different, since the SFR in the bulge is more efficient. Hence, the majority of the bulge novae is produced earlier, at  $T_1$  when the bulge SFR peaks, and therefore they explode earlier. Hence, at  $T_3$  the nova outburst rate in the bulge is already high.

### 4.2. $^{26}\text{Al}$ mass 2D distribution

In this Section, we show the results related to the 2D distribution of  $^{26}\text{Al}$  in the MW within 15 kpc from the galactic center.

In Fig. 4 we report the results from Model 1, where massive stars and nova systems both contribute to the synthesis of  $^{26}\text{Al}$ . In this figure we show the snapshots at the same six times as in Fig. 2. The plots are color coded according to the logarithm of the  $^{26}\text{Al}$  mass in each cell. The indicative location of the solar neighbourhood is suggested by a white-edge star in the left side of each snapshot.

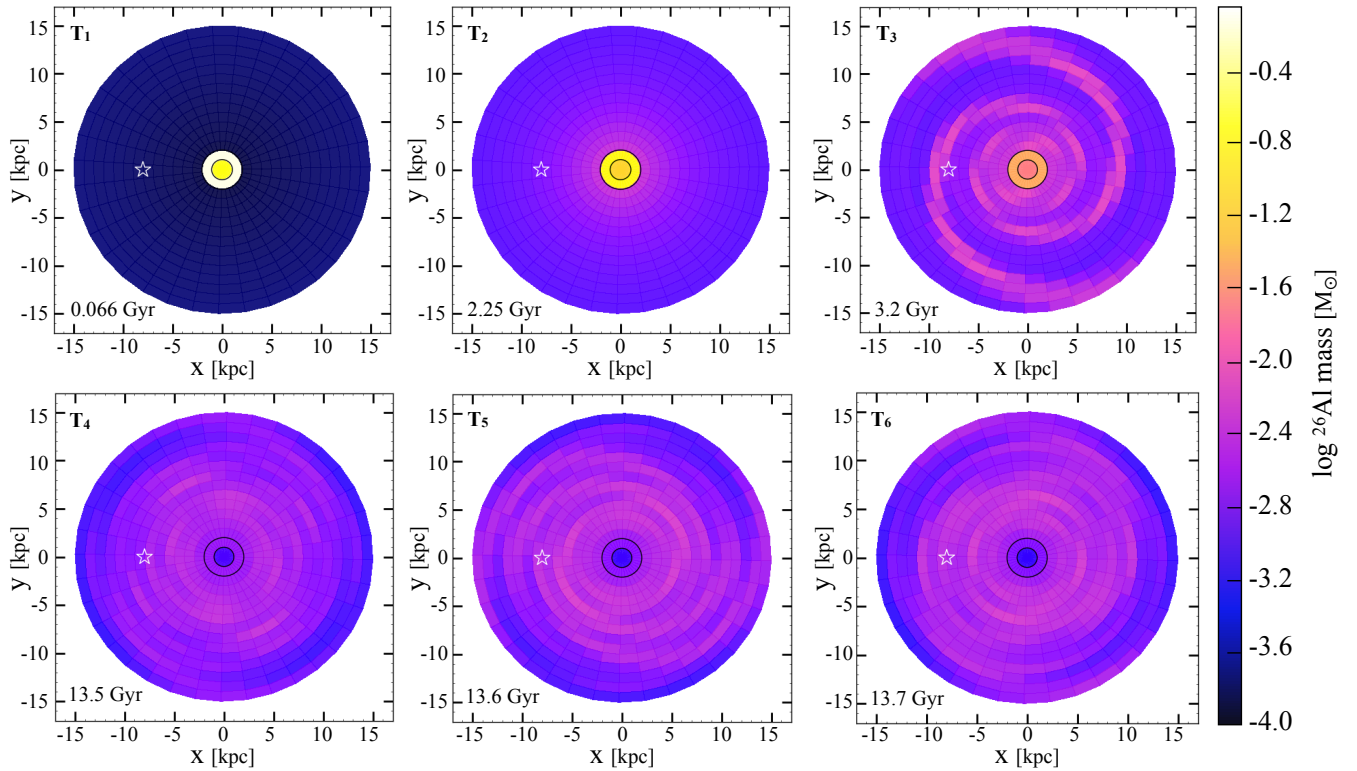


**Fig. 4.** In this panel we show the 2D distribution of  $^{26}\text{Al}$  mass at the six time steps where we have previously analyzed the SFR. In this case we accounted as  $^{26}\text{Al}$  producers both massive stars and novae. The bulge is not represented. Each cell is color coded according to the  $^{26}\text{Al}$  mass contained at that time step and as in Fig. 2 the sun is indicated by the white-edge star.

A comparison between Fig. 4 and the SFR in Fig. 2 is quite interesting. In Fig. 4 the first three panels ( $T_1$ ,  $T_2$  and  $T_3$ ) reproduce perfectly the SFR pattern:

- at  $T_1=0.066$  Gyr the only contribution to  $^{26}\text{Al}$  in the MW comes from the bulge ( $R < 2$  kpc) where the SFR is high, whereas  $^{26}\text{Al}$  in the disc is still very low (as it is the SFR);
- at  $T_2=2.25$  Gyr the SFR in the bulge has already reached a maximum and decreased and the  $^{26}\text{Al}$  shown in the plot has originated from the nova explosions. On the other hand, the SFR in the disc reached the peak, thus causing an increment in the amount of  $^{26}\text{Al}$  produced. Nevertheless, the peak of the  $^{26}\text{Al}$  production in the disc will occur slightly later, due to the delayed contribution from nova systems;
- At  $T_3=3.2$  Gyr, the SFR perturbations have just kicked in and the spiral pattern is accurately reproduced by the  $^{26}\text{Al}$  2D distribution.

These first three panels perfectly mimic the SFR behaviour because after few billion years of evolution, the only significant contribution to the  $^{26}\text{Al}$  comes from the massive stars. Novae contribution will arise at later times, therefore in the first stages of the evolution it is still negligible.

On the other hand, at  $T_4$ ,  $T_5$  and  $T_6$  the scenario is different: in every snapshot the SFR pattern is reproduced with less accuracy and the spiral pattern is recognisable only in the outermost rings. Regarding the present time bulge, the massive stars are almost totally absent and the  $^{26}\text{Al}$  predicted there comes exclusively from recent nova outbursts.

In Fig. 5, where the results from Model 2 are plotted, the scenario is rather different, since novae have been excluded from

the  $^{26}\text{Al}$  nucleosynthesis. The snapshots are taken at the same times, the color coding is the same and the white-edge star still represent the indicative position of the solar neighbourhood.

The first three panels resemble Fig. 4. The only difference is the overall depletion of  $^{26}\text{Al}$  mass over the entire Galaxy due to the removal of the nova systems. The bulge is much less enriched in  $^{26}\text{Al}$  (see  $T_2$  panel) with respect to Fig. 4, since the only contribution in this region was coming from nova systems, that are now excluded. On the other side, the three recent snapshots ( $T_4$ ,  $T_5$  and  $T_6$ ) show a rather good tracing of the SFR since no smoothing from novae is involved. The bulge looks extremely poor in  $^{26}\text{Al}$  since the massive stars are completely absent. The only recent production in the region  $R < 2$  kpc is that coming from AGBs and SNIa.

#### 4.3. $^{26}\text{Al}$ mass azimuthal oscillations

To quantify how much the novae contribute to the scenario we present Fig. 6:

- panel a: we show the SFR at the present time, in the solar ring as a function of the azimuth. The vertical dashed lines mark the peaks of the SFR and are reported in all the panels below. The oscillations are symmetric as was already shown in Fig. 2;
- panel b: we represent the  $^{26}\text{Al}$  mass for Model 1 and Model 2 (pink and green lines respectively). The vertical dashed lines refer to the peaks of the SFR. The oscillations have the same amplitude in the two cases, but, as shown in Fig. 4 and 5, they are far smoother in Model 1 where the spiral pattern at the present time is almost lost. The relative enhancement of the



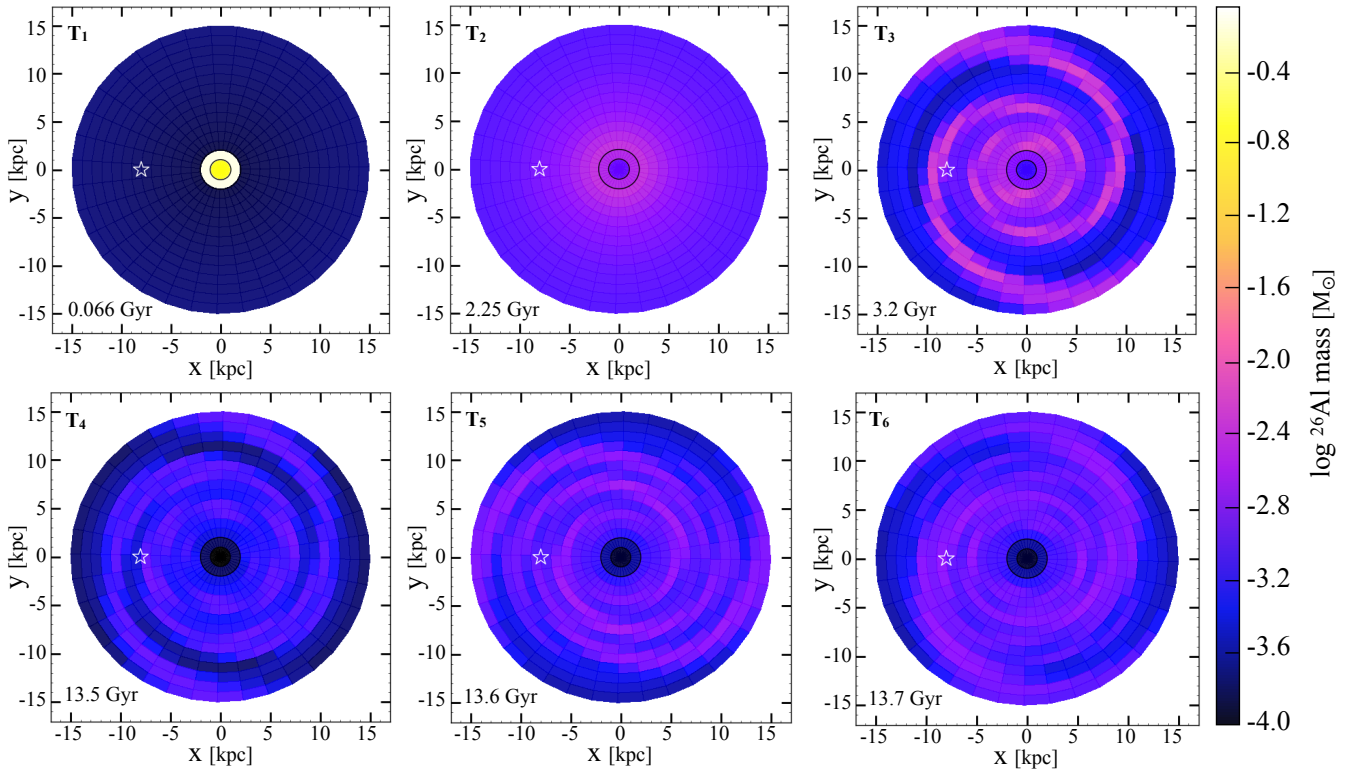


Fig. 5. Same as Fig. 4 but without any contribution from nova systems.

peaks with respect to the minima: for Model 1 the peak is the 28% higher than the minima, whereas in the case of Model 2 the peak is the 150% higher than the minima. The peaks in Model 2 stand out against the background by a factor of  $\sim 5$  more than in Model 1, hence the loss of the spiral pattern;

- panel c: we plot the difference between the  $^{26}\text{Al}$  produced by Model 1 and Model 2. Here we show clearly that the mass of  $^{26}\text{Al}$  produced by novae is dependent on the azimuth but not on the SFR. This value oscillates between 0.004 and 0.006  $M_{\odot}$  and is largest in the minima of the SFR, demonstrating why novae blunt the spiral pattern;
- panel d: here we show the nova distribution in the solar ring, that resembles that of the  $^{26}\text{Al}$  in the previous panel.

#### 4.4. $^{26}\text{Al}$ : predictions versus observations

Regarding the comparison with observational data in Table 2 we report the values of  $^{26}\text{Al}$  within 5 kpc from the Galactic center. Columns from 2-6 report the values in the 1 kpc wide annuli and their sum is listed in column 7. Up to now, the observations performed with COMPTEL and INTEGRAL agreed on the amount of  $^{26}\text{Al}$  present in the MW. Adopting the COMPTEL data [Prantzos & Diehl 1996](#) estimated an  $^{26}\text{Al}$  mass in the range 1.5 - 2.0  $M_{\odot}$  within 5 kpc from the Galactic centre (see also [Diehl et al. 1995](#)). Later, [Diehl 2016](#) estimated  $2.0 \pm 0.3 M_{\odot}$  of  $^{26}\text{Al}$  in the same region after the INTEGRAL data were released.

Within 5 kpc from the Galactic center our Model 1 predicts 1.028  $M_{\odot}$  of  $^{26}\text{Al}$ , whereas Model 2 predicts 0.265  $M_{\odot}$ . In neither of the two cases we are able to recover the exact amount of the  $^{26}\text{Al}$  observed, but a potential solution was proposed by [Della Valle & Izzo \(2020\)](#). The authors report that the nucleosynthesis of the novae in the bulge could be significantly different from

that of the disc novae. The bulge novae could actually eject up to a factor of ten more matter than the disc novae, therefore increasing of the same factor the  $^{26}\text{Al}$  produced. This can be justified by considering that bulge novae exploding now come from very low mass stars that need to accrete a thicker envelope to explode, thus ejecting more matter. By including this additional factor in the calculations, we can reproduce up to 2.882  $M_{\odot}$  of  $^{26}\text{Al}$  with Model 1, therefore with a slightly smaller factor we can reproduce the  $\sim 2 M_{\odot}$  observed.

#### 4.5. Galactic observational constraints

With our choice of input parameters we are able to reproduce the main observational features of the MW disc ( $R > 2$  kpc). We highlight in particular that we can reproduce the current SFR, gas mass, stellar mass, infall rate and both Type Ia and Type II SNe rates.

We report in Table 3 the most important observational constraints in the Galactic disc: in column 2 we show the observed value with the reference, in column 3 the predicted value by our models. We compare our results with the observations from different authors. Regarding the SFR we refer to the values proposed by [Prantzos et al. \(2011\)](#) and [Chomiuk & Povich \(2011\)](#), for the gas mass we rely on [Kubryk et al. \(2015b\)](#), for the stellar mass we compare our results to [Flynn et al. \(2006\)](#), for the infall rate we use the observations by [Marasco et al. \(2012\)](#) and [Lehner & Howk \(2011\)](#) and for the Type II and Type Ia SN rate we refer to [Cappellaro & Turatto \(1997\)](#). We highlight that the two models tested, Model 1 and Model 2, differ only for the nucleosynthesis, therefore the predictions of all the unrelated quantities (such as those listed here) are the same.



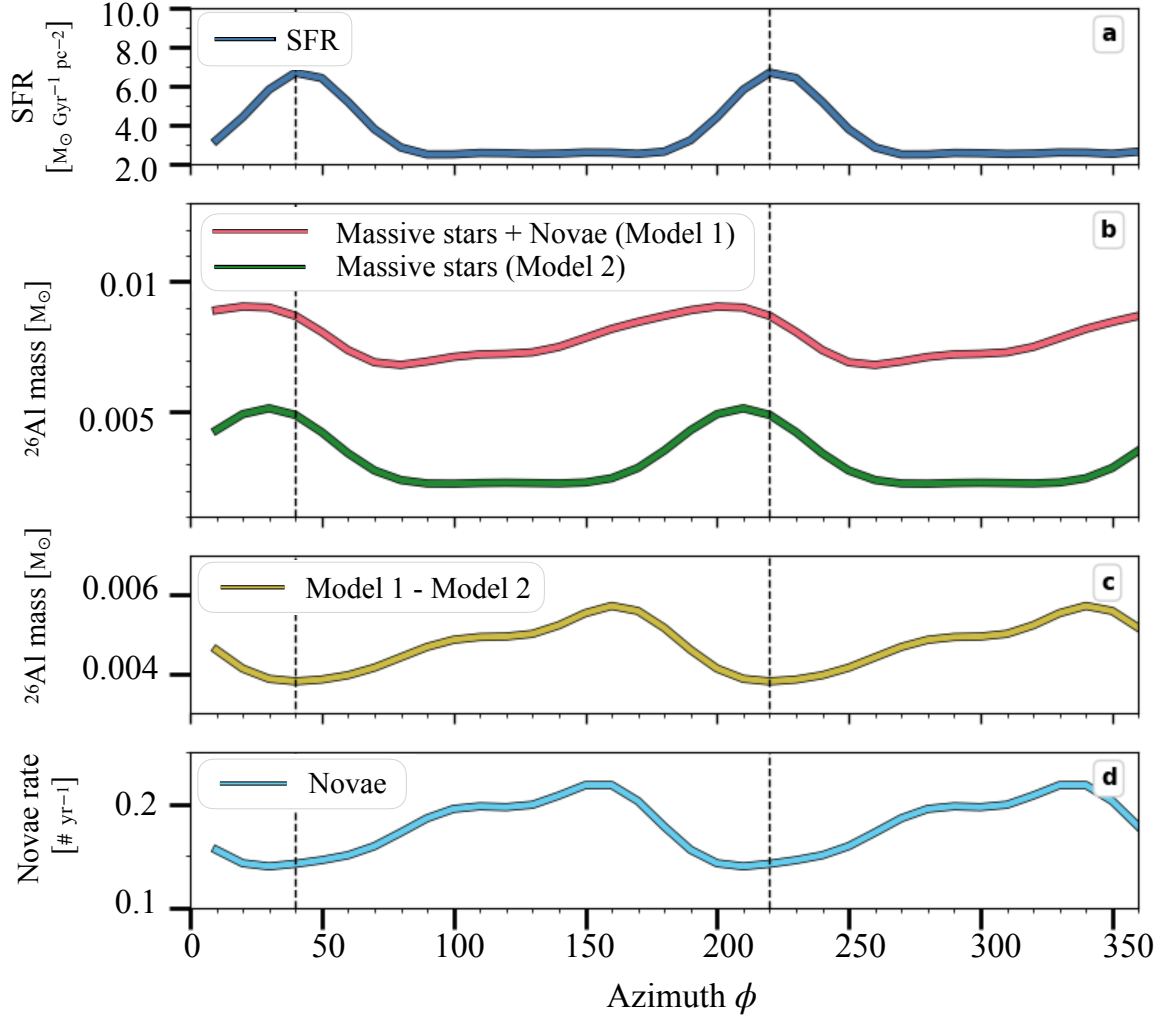


**Fig. 6.** *Panel a:* SFR as a function of the azimuth at the present time and the solar neighbourhood. The black dashed lines, in this plot and in those below, mark the peaks of the SFR. *Panel b:*  $^{26}\text{Al}$  distribution in the solar ring and present time. In pink,  $^{26}\text{Al}$  predicted by Model 1 and in green that from Model 2. *Panel c:* difference between the  $^{26}\text{Al}$  production in the two cases. *Panel d:* novae distribution in the solar ring at the present time.

Model	0 - 1 kpc	1 - 2 kpc	2 - 3 kpc	3 - 4 kpc	4 - 5 kpc	Total (0 - 5 kpc)
<b>Model 1</b>	0.056 $M_{\odot}$	0.150 $M_{\odot}$	0.229 $M_{\odot}$	0.283 $M_{\odot}$	0.312 $M_{\odot}$	1.028 $M_{\odot}$
<b>Model 2</b>	0.006 $M_{\odot}$	0.014 $M_{\odot}$	0.057 $M_{\odot}$	0.083 $M_{\odot}$	0.105 $M_{\odot}$	0.265 $M_{\odot}$

**Table 2.**  $^{26}\text{Al}$  integrated over the five innermost annuli (0 - 5 kpc) at the present time for both models. Column 2-6 report the  $^{26}\text{Al}$  for every single ring (each 1 kpc wide) and column 7 show the total  $^{26}\text{Al}$  within 5 kpc.

## 5. Conclusions

In this paper we model the temporal and spatial evolution of  $^{26}\text{Al}$  in the MW by adopting a 2D chemical evolution model to perform a comparison with the already existing data and a prediction for the upcoming ones. The introduction of a second dimension in the chemical evolution model allows us to investigate how much the approximation of homogeneous mixing affects the production of  $^{26}\text{Al}$ , and which is the relative contribution of novae and massive stars to its mass in the MW. Moreover we can also probe how good the tracing of the SFR is when considering

nova systems as  $^{26}\text{Al}$  producers. We assume the Galaxy to be divided into two main regions: the bulge ( $R \leq 2$  kpc), that is described adopting a homogeneous 1D model, and the disc ( $R > 2$  kpc) where we consider a 2D model, with the SFR being dependent not only on the Galactocentric distance and time but also on the azimuth. The dependency on the azimuth is introduced by applying a perturbation to the 1D SFR, resembling the rotating spiral arm pattern observed in the Galaxy. Our main focus is  $^{26}\text{Al}$ , a short-lived radioisotope with a  $\sim 1$  Myr decay time-scale, generally assumed to be produced by massive stars. These two

	Observations	Predictions
SFR [ $M_{\odot} \text{ yr}^{-1}$ ]	0.65 - 3 (1)	2.24
Gas mass [ $10^9 M_{\odot}$ ]	8.1 - 4.5 (2)	6.4
Stellar mass [ $10^{10} M_{\odot}$ ]	3. - 4. (3)	3.7
Infall rate [ $M_{\odot} \text{ yr}^{-1}$ ]	0.6 - 1.6 (4)	0.65
Type II SNe [events century $^{-1}$ ]	0.4 - 2.0 (5)	0.88
Type Ia SNe [events century $^{-1}$ ]	0.1 - 0.5 (5)	0.2

**Table 3.** MW disc ( $R > 2$  kpc) constraints: in column 2 the observed quantities, in column 3 the predictions from our models. Models 1 and 2 predict the same observables since they differ only on the nucleosynthesis side. **References:** (1) Prantzos et al. (2011), Chomiuk & Povich (2011), (2) Kubryk et al. (2015a), (3) Flynn et al. (2006), (4) Marasco et al. (2012), Lehner & Howk (2011), (5) Cappellaro & Turatto (1997).

facts suggest that  $^{26}\text{Al}$  can be a good tracer of active star formation, therefore its current location in the MW is dependent on the shape of the recent SFR.

With this model we aim at reproducing the observed mass of  $^{26}\text{Al}$  in the Galaxy to investigate the importance of nova contribution to the mass of this element, and studying the effects that novae can produce on  $^{26}\text{Al}$  as tracer of star formation. To do that, we compare two models considering different  $^{26}\text{Al}$  sources: Model 1, where massive stars and nova systems are both responsible for the  $^{26}\text{Al}$  production, and Model 2 where nova systems are excluded. Regarding the yields for both the production sites we adopt the prescriptions of Vasini et al. (2022). By means of our chemical evolution model, we are able to produce 2D maps for the mass of  $^{26}\text{Al}$ , the distribution of massive stars and nova systems in the MW. Our main conclusions can be summarised as follows:

- the nova systems eject nucleosynthesis products with a large time delay due to the initial masses of the binary components and to the time necessary for a white dwarf to cool. Due to this delay, novae are not tracers of the SFR. The maps that we produce show that the peaks of the present time nova distribution at the solar neighbourhood are located in the minima of the present time SFR;
- the two hypotheses about the producers of  $^{26}\text{Al}$  that we test, predict different distributions of the mass of this element. We highlight that when including the production by novae (Model 1), the spiral pattern at the present time is hardly visible, at variance with the case of production from massive stars only (Model 2). In particular, in the case of  $^{26}\text{Al}$  from both production sites, the peaks of the  $^{26}\text{Al}$  distribution are  $\sim 28\%$  higher than the minima, whereas in the case of  $^{26}\text{Al}$  from massive stars only the peaks are  $\sim 150\%$  higher. Therefore, in the case without novae, the peaks of the distribution stand out from the background five times more than in the case with novae included, thus tracing better the spiral arm pattern;
- we compare the  $^{26}\text{Al}$  predicted by the two models with the available observational data, which refer to the innermost 5 kpc of the Galaxy. We integrate the  $^{26}\text{Al}$  within each ring from the center up to 5 kpc and we obtain  $1.028 M_{\odot}$  if novae are included (Model 1) and  $0.265 M_{\odot}$  if novae are excluded (Model 2). Therefore, the relative contribution of novae to the total amount of  $^{26}\text{Al}$  is  $\sim 75\%$  and the other  $\sim 25\%$  comes from massive stars. The observations report  $\sim 2 M_{\odot}$  of  $^{26}\text{Al}$ , hence both our models underestimate the mass of  $^{26}\text{Al}$ . The missing  $^{26}\text{Al}$  mass can be recovered if we consider that bulge

novae can eject up to 10 times more matter than disc novae. Considering a factor of ten, our Model 1 predicts  $2.882 M_{\odot}$  of  $^{26}\text{Al}$  within 5 kpc from the Galactic center, therefore by adopting a factor of  $\sim 6$  we can very well reproduce the observations.

In conclusion, since the tracing of the SFR by  $^{26}\text{Al}$  is lowered by a factor of  $\sim 5$ , if novae are considered, we cannot say that this element is a pure tracer of the SFR. Therefore, other SLRs not produced by novae, such as  $^{60}\text{Fe}$  are more reliable tracers of the SFR.

From the nucleosynthesis side, our 2D chemical evolution model confirms that the nova contribution to  $^{26}\text{Al}$  is fundamental to reproduce the observations especially in the bulge, where they should eject a larger amount of chemical elements as compared to those produced by the disc novae.

## Acknowledgement

A. Vasini and F. Matteucci thank I.N.A.F. for the 1.05.12.06.05 Theory Grant - Galactic archaeology with radioactive and stable nuclei. This research was supported by the Munich Institute for Astro-, Particle and BioPhysics (MIAPbP) which is funded by the Deutsche Forschungsgemeinschaft (DFG, German Research Foundation) under Germany's Excellence Strategy – EXC-2094 – 390783311. F. Matteucci thanks also support from Project PRIN MUR 2022 (code 2022ARWP9C) "Early Formation and Evolution of Bulge and Halo (EFEBHO)" (PI: M. Marconi), funded by the European Union – Next Generation EU. G. Cescutti thanks the support from the PRIN MUR project no. 2022X4TM3H "Cosmic POT" (PI Laura Magrini), also funded by the European Union – Next Generation EU. E. Spitoni and G. Cescutti thank I.N.A.F. for the 1.05.23.01.09 Large Grant - Beyond metallicity: Exploiting the full POTential of CHEMical elements (EPOCH) (ref. Laura Magrini).

## References

- Ballero, S. K., Matteucci, F., Origlia, L., & Rich, R. M. 2007, *A&A*, 467, 123
- Barbuy, B., Chiappini, C., & Gerhard, O. 2018, *ARA&A*, 56, 223
- Bennett, M. & Bovy, J. 2019, *MNRAS*, 482, 1417
- Bird, J. C., Kazantzidis, S., Weinberg, D. H., et al. 2013, *ApJ*, 773, 43
- Brook, C. B., Stinson, G. S., Gibson, B. K., et al. 2012, *MNRAS*, 426, 690
- Cappellaro, E. & Turatto, M. 1997, in *NATO Advanced Science Institutes (ASI) Series C*, Vol. 486, NATO Advanced Science Institutes (ASI) Series C, ed. P. Ruiz-Lapuente, R. Canal, & J. Isern, 77
- Cescutti, G. & Matteucci, F. 2011, *A&A*, 525, A126
- Cescutti, G. & Molaro, P. 2019, *MNRAS*, 482, 4372
- Chiappini, C., Matteucci, F., & Romano, D. 2001, *ApJ*, 554, 1044
- Chomiuk, L. & Povich, M. S. 2011, *AJ*, 142, 197
- Côté, B., Lugaro, M., Reifarh, R., et al. 2019a, *ApJ*, 878, 156
- Côté, B., Yagüe, A., Világos, B., & Lugaro, M. 2019b, *ApJ*, 887, 213
- Cox, D. P. & Gómez, G. C. 2002, *ApJS*, 142, 261
- D'Antona, F. & Matteucci, F. 1991, *A&A*, 248, 62
- Della Valle, M. & Izzo, L. 2020, *A&A Rev.*, 28, 3
- Desch, S. J., Dunlap, D. R., Dunham, E. T., Williams, C. D., & Mane, P. 2023, *Icarus*, 402, 115607
- Diehl, R. 2013, *Reports on Progress in Physics*, 76, 026301
- Diehl, R. 2016, in *Journal of Physics Conference Series*, Vol. 665, *Journal of Physics Conference Series (IOP)*, 012011
- Diehl, R., Dupraz, C., Bennett, K., et al. 1995, *A&A*, 298, 445
- Diehl, R. & Prantzos, N. 2023, *arXiv e-prints*, arXiv:2303.01825
- Flynn, C., Holmberg, J., Portinari, L., Fuchs, B., & Jahreiß, H. 2006, *MNRAS*, 372, 1149
- Ford, H. C. 1978, *ApJ*, 219, 595
- GRAVITY Collaboration, Abuter, R., Amorim, A., et al. 2021, *A&A*, 654, A22
- Grieco, V., Matteucci, F., Pipino, A., & Cescutti, G. 2012, *A&A*, 548, A60
- Iwamoto, K., Brachwitz, F., Nomoto, K., et al. 1999, *ApJS*, 125, 439
- José, J. & Hernanz, M. 2007, *Journal of Physics G Nuclear Physics*, 34, R431
- Karakas, A. I. 2010, *MNRAS*, 403, 1413

- Kennicutt, Robert C., J. 1998, *ApJ*, 498, 541
- Kobayashi, C., Umeda, H., Nomoto, K., Tominaga, N., & Ohkubo, T. 2006, *ApJ*, 653, 1145
- Kroupa, P., Tout, C. A., & Gilmore, G. 1993, *MNRAS*, 262, 545
- Kubryk, M., Prantzos, N., & Athanassoula, E. 2015a, *A&A*, 580, A126
- Kubryk, M., Prantzos, N., & Athanassoula, E. 2015b, *A&A*, 580, A126
- Lehner, N. & Howk, J. C. 2011, *Science*, 334, 955
- Limongi, M. & Chieffi, A. 2006, *ApJ*, 647, 483
- Marasco, A., Fraternali, F., & Binney, J. J. 2012, *MNRAS*, 419, 1107
- Matteucci, F. & Brocato, E. 1990, *ApJ*, 365, 539
- Matteucci, F. & Francois, P. 1989, *MNRAS*, 239, 885
- Matteucci, F. & Greggio, L. 1986, *A&A*, 154, 279
- Matteucci, F., Grisoni, V., Spitoni, E., et al. 2019, *MNRAS*, 487, 5363
- Matteucci, F. & Recchi, S. 2001, *ApJ*, 558, 351
- Meidt, S. E., Rand, R. J., & Merrifield, M. R. 2009, *ApJ*, 702, 277
- Minchev, I., Famaey, B., Quillen, A. C., et al. 2012, *A&A*, 548, A126
- Nofar, I., Shaviv, G., & Starrfield, S. 1991, *ApJ*, 369, 440
- Nomoto, K., Thielemann, F. K., & Yokoi, K. 1984, *ApJ*, 286, 644
- Pleintinger, M. M. M., Diehl, R., Siegert, T., Greiner, J., & Krause, M. G. H. 2023, *A&A*, 672, A53
- Plüscke, S., Diehl, R., Schönfelder, V., et al. 2001, in *ESA Special Publication*, Vol. 459, *Exploring the Gamma-Ray Universe*, ed. A. Gimenez, V. Reglero, & C. Winkler, 55–58
- Prantzos, N., Boehm, C., Bykov, A. M., et al. 2011, *Reviews of Modern Physics*, 83, 1001
- Prantzos, N. & Diehl, R. 1996, *Phys. Rep.*, 267, 1
- Quillen, A. C., Dougherty, J., Bagley, M. B., Minchev, I., & Comparetta, J. 2011, *MNRAS*, 417, 762
- Quillen, A. C. & Minchev, I. 2005, *AJ*, 130, 576
- Roca-Fàbrega, S., Antoja, T., Figueras, F., et al. 2014, *MNRAS*, 440, 1950
- Romano, D. & Matteucci, F. 2003, *MNRAS*, 342, 185
- Salpeter, E. E. 1955, *ApJ*, 121, 161
- Schönfelder, V., Diehl, R., Lichti, G. G., et al. 1984, *IEEE Transactions on Nuclear Science*, 1, 766
- Schulreich, M. M., Feige, J., & Breitschwerdt, D. 2023, *A&A*, 680, A39
- Sellwood, J. A. & Carlberg, R. G. 2014, *ApJ*, 785, 137
- Siegert, T., Pleintinger, M. M. M., Diehl, R., et al. 2023, *A&A*, 672, A54
- Spitoni, E., Cescutti, G., Minchev, I., et al. 2019, *A&A*, 628, A38
- Spitoni, E., Cescutti, G., Recio-Blanco, A., et al. 2023, *A&A*, 680, A85
- Timmes, F. X., Woosley, S. E., Hartmann, D. H., et al. 1995, *ApJ*, 449, 204
- Vasini, A., Matteucci, F., & Spitoni, E. 2022, *MNRAS*, 517, 4256
- Vasini, A., Matteucci, F., Spitoni, E., & Siegert, T. 2023, *MNRAS*, 523, 1153
- Vincenzo, F. & Kobayashi, C. 2020, *MNRAS*, 496, 80
- Wehmeyer, B., López, A. Y., Côté, B., et al. 2023, *ApJ*, 944, 121
- Winkler, C. 1994, *ApJS*, 92, 327
- Woosley, S. E. & Weaver, T. A. 1995, *ApJS*, 101, 181